Journal of Materials Chemistry A

ROYAL SOCIETY OF CHEMISTRY

PAPER

View Article Online
View Journal | View Issue

Cite this: *J. Mater. Chem. A*, 2021, **9**, 17030

Unveiling the crystalline packing of Y6 in thin films by thermally induced "backbone-on" orientation†

Yiqun Xiao,[a] Jun Yuan,[b] Guodong Zhou,[c] Ka Chak Ngan,[a] Xinxin Xia,[a] Jingshuai Zhu,[d] Yingping Zou,[b] Ni Zhao,[c] Xiaowei Zhan[d] and Xinhui Lu*[a]

Received 22nd June 2021
Accepted 9th July 2021

DOI: 10.1039/d1ta05268c

rsc.li/materials-a

Researchers are endeavoring to decode the fundamental reasons for the non-fullerene acceptor, Y6, to deliver high-performance in organic solar cells. In this work, we tackle this problem from the molecular packing point of view. By gradually increasing the thermal annealing temperature of Y6, its backbone order in thin films is significantly enhanced and eventually reoriented to the "backbone-on" orientation with the backbone plane standing on the substrate. It displays well-defined Bragg peaks in two-dimensional grazing-incidence wide-angle X-ray scattering patterns for a clear crystal indexing. The 250 °C annealed pure Y6 and binary PM6:Y6 films exhibit square and rectangular diffraction patterns, respectively. It is suggested that both are polymorphs of two-dimensional Y6 packing in its backbone plane, which resulted from its "L" shaped core-group and the biaxial backbone order through the end-group π–π stacking. Interestingly, the square lattice can be restored in the blend PM6:Y6 film by adding a small amount of IDIC. However, on the other hand, a larger portion of IDIC in the ternary blend hinders the long-range crystalline packing of Y6 and correlatedly deteriorates the device performance. This work provides an in-depth understanding of the molecular packing mechanism of Y6 in thin films for the future rational design of high-performance organic photovoltaic molecules with advantageous crystalline packing motifs.

Introduction

Nowadays, organic solar cells (OSCs) are playing an increasingly important role in photovoltaic (PV) technology, thanks to its intrinsic advantages including solution-processability, non-toxicity, lightweight, semitransparency and flexibility. Recent advancements in the device efficiency of OSCs are mainly due to the prosperous development of non-fullerene acceptors (NFAs), which offer great energy levels and morphology tunability.[1–7] Since the synthesis of the landmark NFA-ITIC by Zhan and co-workers in 2015,[8] the power conversion efficiency (PCE) of single-junction OSCs was progressively promoted to over 14%.[9–12] In 2019, the PCE of OSCs made a further big step forward due to the invention of another milestone NFA-Y6 by Zou group.[13] Y6 employs a unique "L"-shaped core-group of a benzothiadiazole unit attached with fused rings (dithienothiophen[3.2-*b*]-pyrrolobenzothiadiazole) on both sides forming a DAD structure, which gives rise to a narrowed bandgap. Moreover, fabricating Y6-based ternary OSCs further improves PCE as it not only enhances the photocurrent by broadening the absorption spectrum but also provides more morphology-tuning handles.[14–18] Based on Y6 and its derivatives, the single-junction OSC efficiency has been pushed over 18% to date.[14,16,19–25]

Alongside improving PCE, researchers also endeavor to understand the fundamental structural reasons for Y6 and its derivatives to deliver high efficiencies. In the paper that Zou *et al.* first reported Y6,[13] our group contributed grazing-incidence wide-angle X-ray scattering (GIWAXS) characterization and observed two blur scattering peaks in the in-plane (IP) direction and suggested that there exists the backbone order of Y6 due to its end group π–π stacking similar to that observed in ITIC and derivatives.[26,27] Furthermore, a variety of single-crystal studies have provided insightful understanding about the superior crystal structure of Y6. For instance, Liu group reported that Y6 could form a zig–zag polymer-like conjugated structure along the backbone in the single crystal.[28] Yip *et al.* using molecular dynamics (MD) simulations and single-crystal analysis demonstrated that the versatile dimers formed by distinctive π–π stacking of Y6 not only exist in the single crystals but also in thin films.[29] Furthermore, Jen and coworkers reported the existence of backbone overlapping *via* the π–core

[a]*Department of Physics, The Chinese University of Hong Kong, Sha Tin, New Territories, Hong Kong, China. E-mail: xinhui.lu@cuhk.edu.hk*

[b]*College of Chemistry and Chemical Engineering, Central South University, Changsha 410083, PR China*

[c]*Department of Electronic Engineering, The Chinese University of Hong Kong, Sha Tin, New Territories, Hong Kong, PR China*

[d]*School of Materials Science and Engineering, Peking University, Beijing 100871, China*

† Electronic supplementary information (ESI) available: Mobility measurements and photoluminescence spectra. See DOI: 10.1039/d1ta05268c

interaction of Y6 in addition to the end group π–π stacking.[30] Despite collective results obtained from single-crystal analysis and simulations, the molecular packing motif as a result of the backbone order of Y6 has not been directly observed and fully understood in thin films.

Here, we report the detailed molecular packing motif of Y6 in pure and blended thin films with the help of GIWAXS and thermal annealing. Thermal annealing is an effective means to enhance the crystallinity of organic thin films.[31–33] When the annealing temperature is increased crossing or approaching the transition temperatures, long-range diffusion will be activated and substantially promote the crystallization of organic molecules.[34–38] Therefore, we observe that the backbone order of Y6 in thin films is significantly enhanced and eventually reoriented from IP to the out-of-plane (OOP) direction by gradually elevating the thermal annealing temperature. Consequently, the scattering signals corresponding to the backbone order of Y6, which are originally folded along the q_r axis, now display a well-defined two-dimensional (2D) diffraction pattern in the q_r–q_z plane, allowing a clear crystal indexing of Y6-based films for the first time. The 250 °C annealed pure Y6 and binary PM6:Y6 films exhibit square and rectangular diffraction patterns, respectively. Both are polymorphs of 2D Y6 crystalline packing resulting from its "L"-shaped core-group and the biaxial backbone order through the end-group π–π stacking. Interestingly, the square lattice can be restored by adding a small amount of IDIC[39] into the PM6:Y6 film. The incorporation of IDIC may reduce the intermixing between PM6 and Y6 and promote the packing of Y6 as it is in the pure film. However, a higher concentration of IDIC hinders the crystalline packing of Y6. Hence, the ternary PM6:Y6:IDIC (1 : 1 : 0.2) device experiences a significant deterioration compared with binary PM6:Y6 and ternary PM6:Y6:IDIC (1 : 1.15 : 0.05) devices. This work reveals molecular packing motifs of Y6 in thin films for the first time and explains the advantageous crystalline packing of Y6-like organic molecules with the "L"-shaped core group, providing insights into future rational designs of high-performance organic PV molecules.

Results and discussion

The chemical structure of Y6 is shown in Fig. 1a. Unlike ITIC family molecules,[8,39] which usually has a linear-shaped core group, Y6 possesses an "L" shape core group, which governs its molecular packing configuration. Employing GIWAXS, thin films of pure Y6, ~100 nm thick, thermally annealed at different temperatures up to 250 °C were investigated. The decomposition temperature of Y6 is ~318 °C as reflected in the thermogravimetric analysis (TGA) (Fig. S1a†) and the reported work,[13] suggesting that annealing temperatures of up to 250 °C will not decompose Y6. We present 2D GIWAXS patterns of pure Y6 films annealed at different temperatures in Fig. 1b–f and the corresponding line-cuts in Fig. 1g and h. The as-cast (25 °C) and 95 °C annealed films exhibit similar GIWAXS patterns with two weak and broad scattering peaks centered at $(q_r, q_z) = (0.290, 0)$ and (0.410, 0) Å^{-1}, where $q_r = \sqrt{q_x^2 + q_y^2}$ in the IP direction and a π–π peak at (0, 1.75) Å^{-1} ($d = 3.59$ Å) in the OOP direction, indicating a dominant face-on orientation, which is consistent with previous reports.[13,28,29] The scattering peaks become noticeably sharpened when the films are annealed at or above 200 °C, demonstrating that structural order of Y6 can be progressively enhanced by thermal annealing. At 220 °C, the π–π peak further increases and shifts slightly to a larger q_z of 1.77 Å^{-1} ($d = 3.55$ Å), signifying a little tighter π–π stacking as a result of crystallinity increase. Intriguingly, the scattering peak at (0.290, 0) Å^{-1} splits into two sharp peaks at (0.280, 0) and (0.310, 0) Å^{-1}, implying an increase of peak resolution due to the growth of long-range crystalline domains. Besides, new peaks emerge at (0.420, 0) and (0.550, 0) Å^{-1}, indicating further enhancement of structure order in the backbone plane of Y6, because it is orthogonal to the π–π stacking direction. However, these peaks are located in the q_x–q_y plane, which is folded along the q_r axis of the GIWAXS pattern, challenging the clear indexing of the packing motif. Fortunately, the 250 °C annealing reorients the structure order in the backbone plane from the IP to the OOP direction, as indicated by the appearance of the π–π peak along the q_r axis at (1.77, 0) Å^{-1}. Well-defined Bragg peaks are now displayed in the q_r–q_z plane (Fig. 1f). The reorientation of organic molecules under thermal annealing has been observed previously,[40,41] which was attributed to the long-range diffusion of molecules activated by heat. Differential scanning calorimetry (DSC) of Y6 show a tiny endothermic peak at ~236 °C (Fig. S1b†), which might be the signal of such a transition.

We then index the GIWAXS pattern of the 250 °C annealed Y6 film in detail. Following the convention,[42,43] we use b axis and the Miller index k for the structural order along the π–π stacking direction and label the peak at (1.77, 0) Å^{-1} as the (010) peak with a lattice constant $b = 3.55$ Å (Fig. 1f). The enlarged GIWAXS pattern (Fig. 2a) in the small q region presents a square diffraction pattern as illustrated in Fig. 2b with $a^* = c^* = 0.140$ Å^{-1}, corresponding to a square lattice with $a = c = 44.8$ Å (Fig. 2c). Note that not all the Bragg peaks are shown on the reciprocal lattice, which is likely due to the systematic absence caused by the complicated structure factor. Since a and c have the same lattice constants, it is unlikely for them to align with the lamellar and backbone directions, as observed in ITIC derivatives.[26,27] Based on the molecular structure of Y6, we find that two Y6 molecules with a "zig–zag" π–π stacking (Fig. 2d) of the end groups will exhibit a matching lattice constant. Furthermore, the direction of this structure order can rotate 90° through an "armchair"-like end group π–π stacking of Y6, forming an "L"-shaped building block and ultimately a square lattice, as illustrated in Fig. 2e and f. This unique packing motif should be a direct consequence of Y6's L-shaped core-group and its biaxial backbone order through the end-group π–π stacking. To distinguish the packing orientation of the 250 °C annealed Y6 film from the conventional "face-on" and "edge-on" orientation, we call it "backbone-on" since it has the 2D backbone plane "standing" on the substrate. The proposed packing motif also works for the 220 °C annealed film, in which the 2D square lattice lies in the IP direction exhibiting folded diffraction peaks

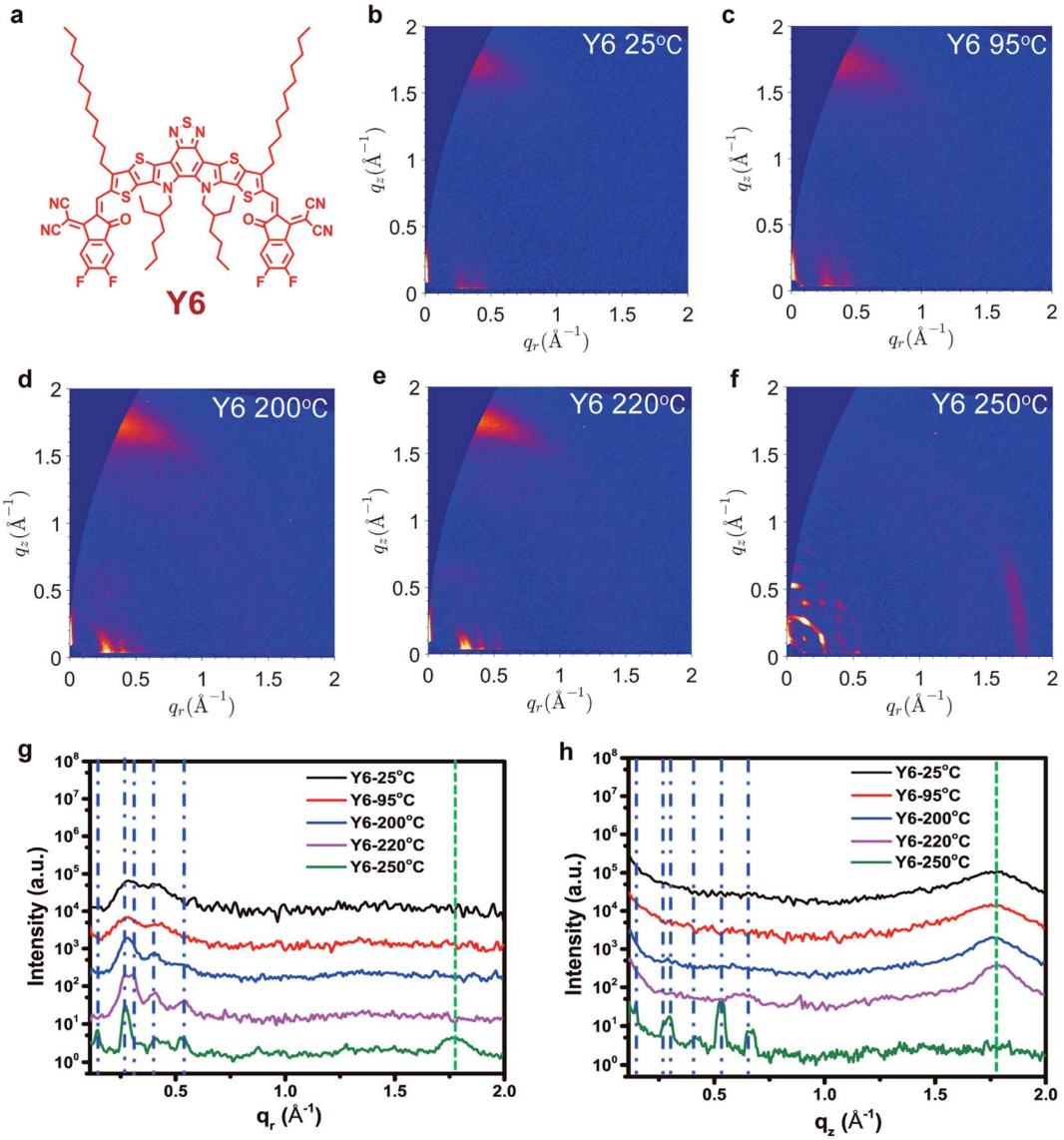

Fig. 1 (a) Chemical structure of Y6; 2D GIWAXS pattern of the (b) as cast and thermal annealed at (c) 95 °C, (d) 200 °C, (e) 220 °C and (f) 250 °C pure Y6 films, respectively. Corresponding intensity profiles along (g) IP and (h) OOP directions.

along the q_r axis due to face-on orientation. The peaks at (0.280, 0), (0.310, 0), (0.420, 0) and (0.550, 0) Å^{-1} can be indexed as (200), (201), (300) and (400) peaks, respectively. Note, these peaks also appear in the scattering pattern of the 250 °C-annealed Y6 film, suggesting the co-existence of backbone-on and face-on oriented Y6 molecules. Tracing back to the scattering patterns of as-cast and low-temperature annealed films, the two broad peaks observed along the q_r axis also agree with the proposed packing motif, suggesting the existence of 2D backbone-packing structure, albeit at a shorter range.

To investigate the molecular packing motif of Y6 in blend films, we fabricated a series of blend films of PM6:Y6:IDIC by fixing the mass ratio of donor and acceptor to 1 : 1.2 but varying the ratios of Y6:IDIC. All the films are annealed at either 95 °C (a common device annealing temperature[13,14]) or 250 °C. The chemical structures and GIWAXS patterns of pure PM6 and IDIC films are included in Fig. S2 and S3.† In contrast to Y6, there is no obvious lattice reorientation, but the higher crystallinity observed in pure PM6 and IDIC films annealed at 250 °C. Fig. S4† shows GIWAXS patterns of blend films annealed at 95 °C. They exhibit similar scattering patterns with a lamellar peak at (q_r, q_z) = (0.290, 0) Å^{-1} (d = 21.7 Å) and a π–π peak at (0, 1.72) Å^{-1} (d = 3.65 Å), which are mainly originated from crystalline PM6 domains. TGA results suggest that no decomposition happened for PM6 and IDIC below 300 °C either (Fig. S1†). Therefore, we can also apply high-temperature thermal annealing to promote the crystalline packing of Y6 in the blend films.

Fig. 3a–d and S5† present GIWAXS patterns and the corresponding line-cuts of all binary and ternary blend films annealed at 250 °C, respectively. In these patterns, peaks at ~(0.290, 0) and (0, 1.70) Å^{-1} are assigned to the lamellar and π–

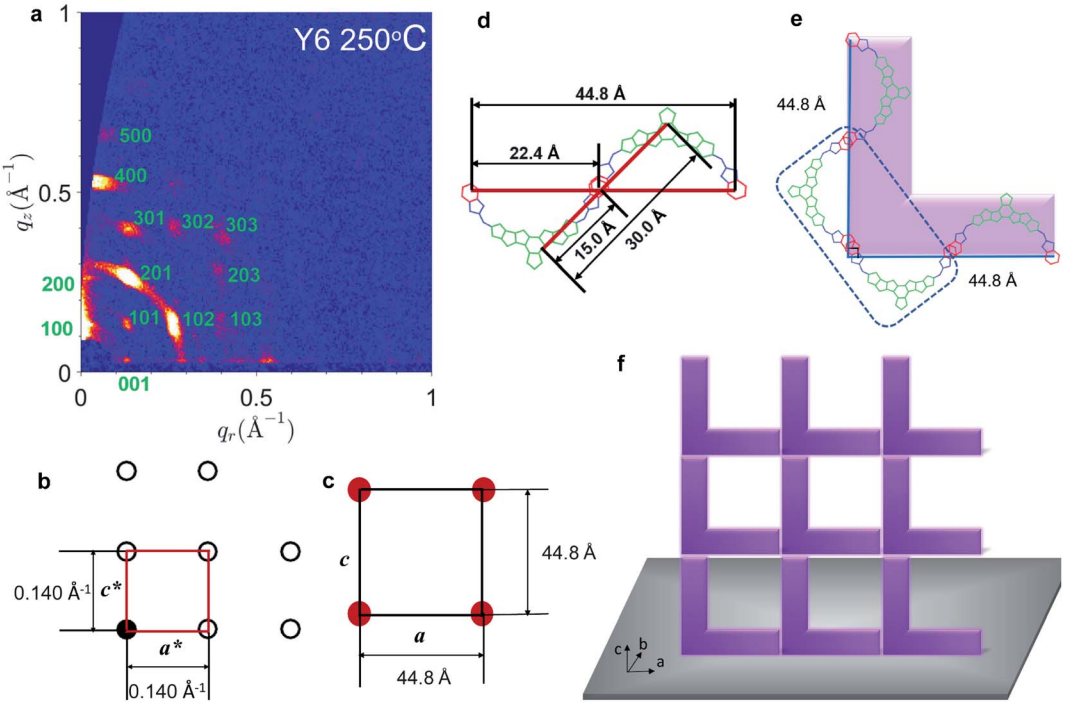

Fig. 2 (a) Enlarged picture in small q region of Y6 pattern at 250 °C with peaks indexed; (b) scattering pattern obtained from the Bragg peaks shown in (a). The filled circle corresponds to the origin; (c) the corresponding real-space lattice obtained from the scattering pattern; (d) schematics of "zig–zag" shaped Y6 dimers with characteristic molecular order spacings and corresponding scattering peaks; (e) "L" shaped building blocks connected by Y6 dimers; (f) cartoon of square Y6 molecular packing networks formed by the "L" shaped building blocks.

π stacking of face-on oriented PM6, respectively, while other peaks should originate from Y6 or IDIC crystalline domains. The GIWAXS patten of the binary PM6:Y6 film annealed at 250 °C (Fig. 3a) demonstrates well-defined Bragg peaks, implying that the strong backbone-on orientation can also be promoted in the binary PM6:Y6 film by thermal annealing. The scattering peaks can be indexed by a rectangular lattice with the unit cell constants of $a = 30.0$ Å and $c = 57.1$ Å (Fig. 3e and f). Moreover, they span relatively larger polar angles as compared with the peaks observed in pure Y6 films, implying a slight reduction of orientational order due to the mixing with PM6. There are also scattering peaks folded along the q_r axis, indicating the existence of both face-on and backbone-on oriented crystalline domains. Obviously, Y6 molecules in the 250 °C annealed binary PM6:Y6 film still form a long-range ordered 2D structure in the backbone plane but in a different way from that in the pure Y6 film. Based on its lattice constants, we propose that the rectangular unit cell is formed by "armchair"—"zig–zag"—"armchair" connected Y6 molecules, while the square unit cell is formed by "zig–zag"—"armchair"—"zig–zag" connected Y6 molecules, as illustrated in Fig. 3g and j. Interestingly, the ternary PM6:Y6:IDIC (1 : 1.15 : 0.05) blend film restores the square lattice packing of Y6 as observed in the pure film (Fig. 3h–j). However, the PM6:Y6:IDIC (1 : 1 : 0.2) blend film (Fig. 3c) exhibits no apparent scattering features from Y6, suggesting that the crystalline packing of Y6 is disturbed with more incorporation of IDIC. Fig. 3l summarizes the highly-ordered molecular packing of Y6 in the rectangular and square lattices. Both rectangular and square lattices should be polymorphs of 2D crystalline packing of Y6 in its backbone plane, owning to their strong backbone order with "zig–zag" and "armchair" end-group π–π stacking, which is in agreement with previous MD simulation results.[29] To generalize this hypothesis to other acceptors with this feature, we have investigated the molecular packing of another DAD–core NFA, BTP-2F-ThCl.[23] GIWAXS patterns and the corresponding intensity profiles of pure BTP-2F-ThCl films annealed both at 95 °C and 250 °C are presented in Fig. S6.† The scattering pattern of 250 °C annealed BTP-2F-ThCl film can be well indexed with the same rectangle lattice, indicating that this molecule also has the same packing motif as Y6 due to the L-shaped core structure.

The molecular packing of organic semiconducting materials in the active layer is known to be correlated with the charge transport properties and the device performance.[44] Although the packing motif of Y6 was determined from the films annealed at 250 °C, the two broad peaks observed along the q_r axis in the as-cast and low-temperature (≤200 °C) annealed films also agree with the proposed packing motif, suggesting the existence of 2D backbone packing structure, albeit in a shorter range. Therefore, we investigate the structure–performance correlation of 95 °C annealed film, as it is the most commonly reported annealing temperature in previous works.[13,14] Firstly, space charge limited current (SCLC) (Fig. S7†) and field-effect transistor (FET) methods (Fig. S8†) were employed to estimate OOP and IP electron mobilities of the blend films, respectively, which critically influences charge

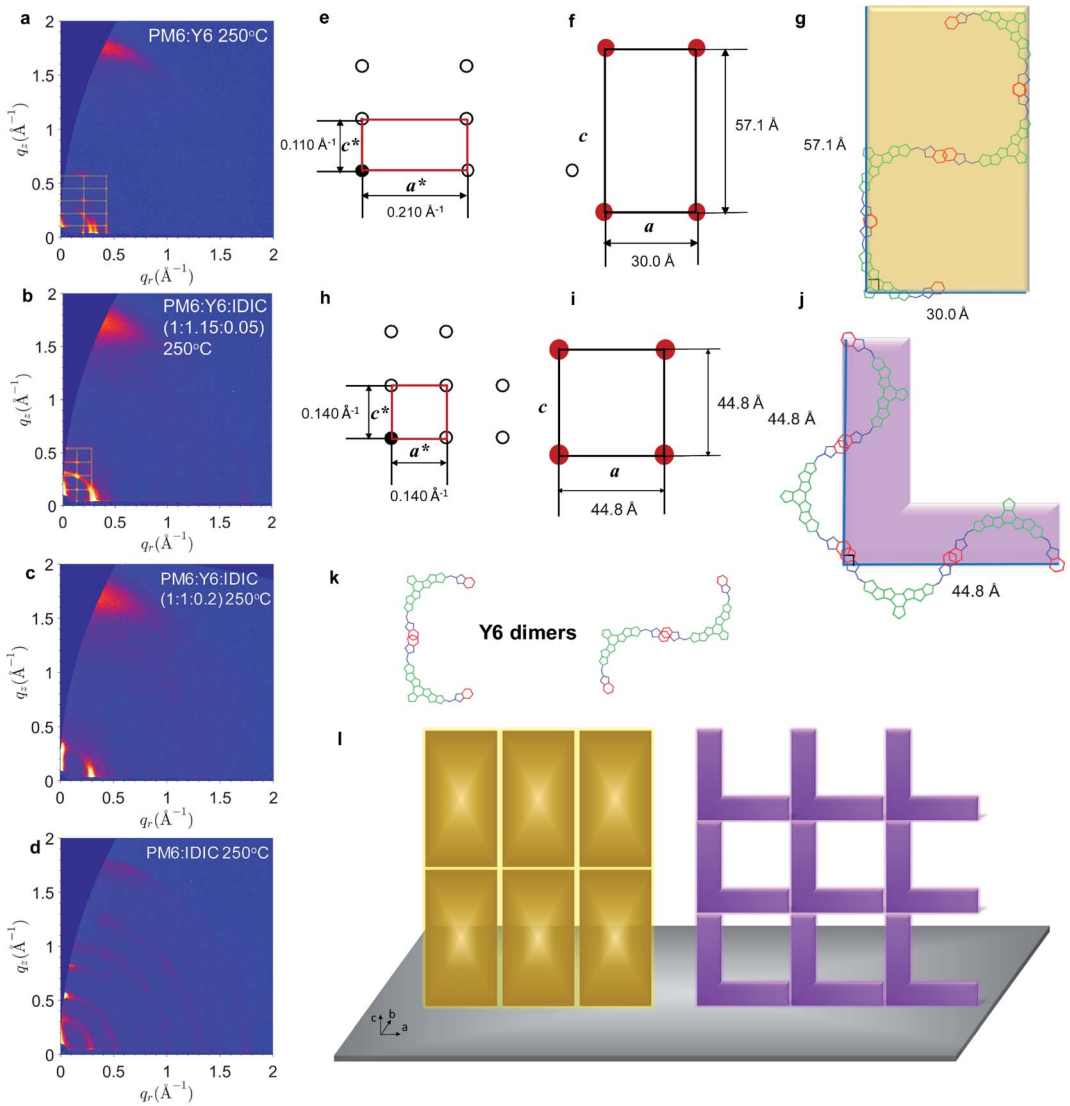

Fig. 3 2D GIWAXS pattern of (a) PM6:Y6, (b) PM6:Y6:IDIC (1 : 1.15 : 0.05), (c) PM6:Y6:IDIC (1 : 1 : 0.2) and (d) PM6:IDIC blend films annealed at 250 °C; (e) scattering pattern and (f) the corresponding real-space unit cell of Fig. 4a; (g) Y6 building blocks of the molecular packing in binary PM6:Y6 film; (h) main scattering pattern and (i) the corresponding real-space unit cell extracted from Fig. 4b; (j) Y6 building blocks of the molecular packing in ternary PM6:Y6:IDIC (1 : 1.15 : 0.05) film; (k) "zig–zag" and "rectangle" shaped Y6 dimers; (l) a schematic view of the 2D molecular packing networks of Y6 with rectangle and square lattices in the blend films.

transport and recombination, and in turn the fill factor (FF) and short circuit current density (J_{SC}) of the devices.[45] The extracted IP and OOP electron and hole mobilities are shown in Tables S1 and S2.† The ternary PM6:Y6:IDIC (1 : 1.15 : 0.05) film shows the highest electron mobility ($\mu_e = 1.49 \times 10^{-3}$ cm^2 V^{-1} s^{-1}) in the IP direction, benefitting from the restored highly biaxial backbone-order observed in the high-temperature GIWAXS pattern. Although the π–π stacking in the *b* axis is not necessarily forming 3D unit cells with the 2D lattice in the backbone plane, it can still couple with the 2D lattice to create efficient 3D electron transport pathways. On the contrary, the PM6:Y6:IDIC (1 : 1.0 : 0.2) film exhibited the lowest electron mobility, which may be attributed to the hindered long-range molecular packing of Y6. The UV-vis light absorption spectra (inset: energy level alignment) of pure PM6, Y6 and IDIC films and blend films are shown in Fig. 4a and S9b,† respectively, demonstrating that they have complimentary light absorption spectra suitable for ternary devices. Solar cells were fabricated in a conventional device structure of ITO/PEDOT:PSS/active layer/PNDIT-F3N/Ag (Fig. S9a†). Current density–voltage (*J*–*V*) curves of typical devices are plotted in Fig. 4b with the corresponding photovoltaic parameters listed in Table 1. The external quantum efficiency (EQE) spectra of the best devices are shown in Fig. 4d and the integrated current densities are also presented in Table 1. The integrated current densities from the EQE spectra of all devices are in good consistency (within 5% difference) with the J_{SC} from *J*–*V* curves. The best binary PM6:Y6 device shows a PCE of 16.19%, akin to the previously reported performance.[13,45] The other binary PM6:IDIC device exhibits a PCE of 10.77% with a higher V_{OC} of 0.944 V due to its relatively higher LUMO

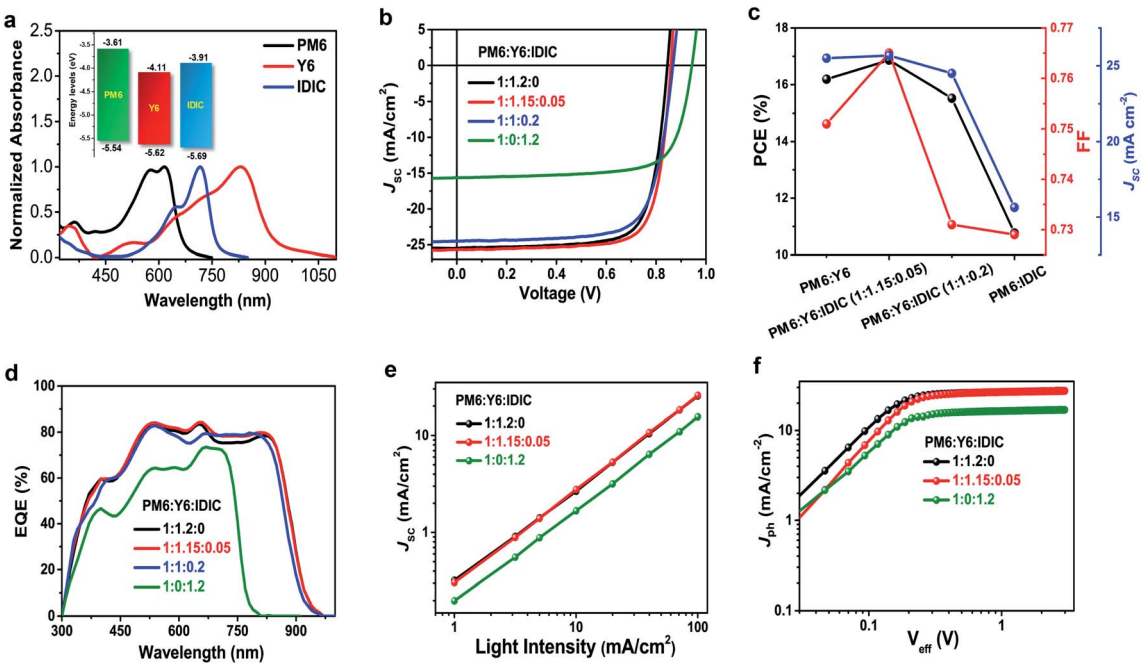

Fig. 4 (a) UV-vis light absorption spectra of PM6, Y6, IDIC (inset: energy level alignment diagram); (b) J–V curves, (c) diagram of parameters including PCE, FF and J_{SC} and (d) EQE spectra of binary and ternary films based on PM6:Y6:IDIC with different mass ratios; (e) J_{SC} *versus* P_{light} and (f) J_{ph}–V_{eff} curves of the binary and optimized ternary OSCs.

level.[13,46] As expected, the champion device was achieved by the ternary PM6:Y6:IDIC (1 : 1.15 : 0.05) blend, demonstrating a PCE as high as 16.86% with a V_{OC} of 0.859 V, a J_{SC} of 25.67 mA cm^{-2}, and a FF of 76.5%, consistent with the observed highest electron and most balanced electron/hole mobilities. In contrast, the PM6:Y6:IDIC (1 : 1 : 0.2) device experiences a noticeable drop in J_{SC} and FF, as shown in Fig. 4c, consistent with the observed disrupted molecular packing of Y6 with more incorporation of IDIC. Despite deteriorated performance at high annealing temperatures, Y6-based devices fabricated at the same temperature still show the same trend as shown in Fig. S10, Tables S3 and S4.† The ternary PM6:Y6:IDIC (1 : 1.15 : 0.05) device exhibited a relatively highest FF, while the values for the ternary PM6:Y6:IDIC (1 : 1 : 0.2) device was the lowest, in correlation with the observed molecular packing of Y6. Note here, the optimized mass ratio of the ternary blends is not the same as that reported in previous literature,[47,48] possibly due to differences in material batches and film processing details.[49] The evolution of J_{SC} under different incident light intensities (P_{light}) is plotted in Fig. 4e to study the charge recombination mechanism in PM6:Y6, PM6:Y6:IDIC (1 : 1.15 : 0.05) and PM6:IDIC devices. The S values for PM6:Y6, PM6:Y6:IDIC (1 : 1.15 : 0.05) and PM6:IDIC blends are fitted to be 0.955, 0.967, and 0.949, respectively, in accordance with the trend of FF. It is suggested that bimolecular recombination is effectively reduced in the ternary PM6:Y6:IDIC (1 : 1.15 : 0.05) device as a result of the enhanced structural order of Y6. Moreover, Fig. 4f displays the photocurrent ($J_{ph} = J_L - J_D$, where J_L/J_D are current density in light/dark) at an effective voltage ($V_{eff} = V_{appl} - V_0$, where V_0 is the voltage when $J_L = J_D$ and V_{appl} is the applied bias voltage). At a very high effective voltage, all the dissociated charges are assumed to reach the corresponding electrodes forming a saturated photocurrent J_{sat}. The charge generation and collection efficiencies extracted are summarized in Table S5,† which indicates that favorable long-range order of Y6 with small incorporation of IDIC could benefit charge dissociation and collection.

Furthermore, grazing-incidence small-angle X-ray scattering (GISAXS) provides further insights into the phase separation behaviors of blend films annealed at 95 °C (Fig. 5). By fitting the scattering profiles with the previously reported models,[50] the averaged intermixing and pure acceptor phase domain sizes

Table 1 Device performance of the binary and ternary OSCs

PM6:Y6:IDIC	V_{OC}[a] (V)	J_{SC}[a] (mA cm^{-2})	J_{SC}[b] (mA cm^{-2})	FF[a] (%)	PCE[a] (%)
1 : 1.2 : 0	0.845 (0.841 ± 0.006)	25.49 (25.13 ± 0.24)	24.98	75.1 (74.9 ± 0.4)	16.19 (15.83 ± 0.20)
1 : 1.15 : 0.05	0.859 (0.855 ± 0.005)	25.67 (25.51 ± 0.17)	25.38	76.5 (75.7 ± 0.7)	16.86 (16.51 ± 0.13)
1 : 1 : 0.2	0.868 (0.864 ± 0.007)	24.49 (24.14 ± 0.15)	24.24	73.1 (73.0 ± 0.6)	15.53 (15.23 ± 0.16)
1 : 0 : 1.2	0.944 (0.939 ± 0.006)	15.64 (15.24 ± 0.26)	14.92	72.9 (72.2 ± 0.7)	10.77 (10.33 ± 0.25)

[a] Averaged values by 20 devices in brackets. [b] Integrated J_{SC}s obtained from the EQE spectra.

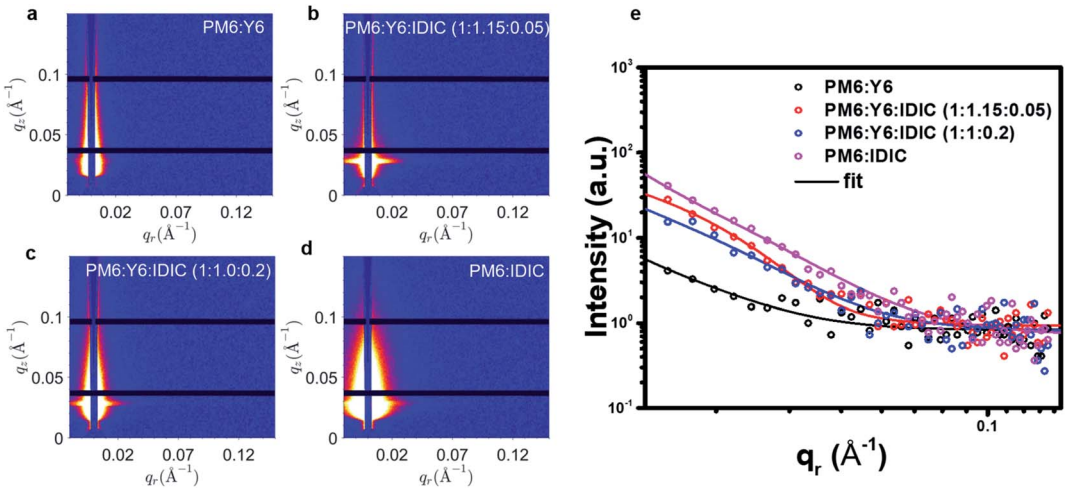

Fig. 5 (a–d) 2D GISAXS patterns of the blend films; (e) intensity profiles along IP direction of GISAXS pattern with the best fittings.

were extracted and summarized in Table S6.† Comparing the PM6:Y6 and PM6:Y6:IDIC (1 : 1.15 : 0.05) films, the average size of intermixing domains decreases from 49 nm to 38 nm, while the pure acceptor phase domains increase from 17 nm to 22 nm, beneficial to the charge dissociation and collection. Contact angle measurements (Fig. S11†) with the surface tension values (γ) calculated in Table S7† using the Flory–Huggins model[51] indicated that the miscibility between IDIC and Y6 is relatively better than that between PM6 and Y6, suggesting that Y6 molecules tend to mix with IDIC rather than PM6 in the ternary film, which may drive the phase separation between PM6 and Y6 and the intermixing of IDIC and Y6 in the ternary films. Therefore, we propose a possible scenario to explain the observed distinct packing motif of Y6 in the blend films; the interaction between PM6 and Y6 causes a different packing motif of Y6 from that in its pure film. The addition of IDIC promotes the formation of larger pure acceptor domains. When the content of IDIC is low, pure Y6 domains are dominant, this tendency will promote the phase separation between PM6 and Y6, therefore restoring its packing motif as in the pure film due to larger pure phase domains. When the content of IDIC becomes high, the intermixing of the two NFAs which possess largely distinctive packing motifs, Y6 and IDIC, instead suppresses the long-range crystalline packing of Y6 in the 250 °C annealed PM6:Y6:IDIC (1 : 1 : 0.2) blend film.

To further confirm the generality of our conclusion with other donor polymer and secondary acceptor, we extended the systems to a new secondary acceptor and a new donor. Firstly, the secondary acceptor IDIC was replaced with ITIC-Th, since ITIC-Th also has a linear core as well as the linear backbone ordering as IDIC.[26] The GIWAXS patterns of PM6:Y6:ITIC-Th at different mass ratios of acceptors and the corresponding intensity profiles of the 250 °C-annealed blend films are shown in Fig. S12.† At a mass ratio of 1 : 1.15 : 0.05, the GIWAXS pattern also exhibits sharp and discrete Bragg peaks, which can be indexed by the rectangular lattice as observed in the binary PM6:Y6 film. At a mass ratio of 1 : 1 : 0.2, the excessive ITIC-Th also disturbs the long-range order of Y6, akin to that in the ternary PM6:Y6:IDIC system, which is also in good accordance with the low-temperature annealed device trend of previously reported works.[52] Furthermore, the donor polymer PM6 was substituted with PTQ10.[53] Different from PM6 based films, PTQ10-based blend films exhibit the square lattice packing of Y6 in both binary and ternary films (Fig. S13†). Therefore, it is suggested that both the square lattice and the rectangular lattice are generally polymorphs of Y6-like molecules. The choice of the donor polymer or the second acceptor may influence the crystallization pathway of Y6, which leads to any of these polymorphs.

In summary, we report a molecular packing motif of Y6 in pure and blend films by thermal-enhanced crystal growth and reorientation. Interestingly, the packing motifs of Y6 are noticeably different in the pure and binary blend films, exhibiting square or rectangular lattices, respectively. Both lattices are polymorphs of Y6 crystalline packing with "zig–zag" and "armchair" types of end group π–π stacking. A small amount of IDIC could help restore the square lattice packing motif of Y6 in its pure film, while a large amount of IDIC, on the other hand, will suppress Y6's crystalline packing. It is further supported by the mobility and device data that the ternary PM6:Y6:IDIC (1 : 1.15 : 0.05) device experiences remarkable improvements in electron transport and consequently device performance. The unique crystalline packing of Y6 is a direct consequence of its L-shaped core group, which enables the biaxial backbone stacking to form 2D electron transport pathways in the backbone plane. Further exploration in the detailed packing motifs of other acceptors in this group will for sure draw more insights to guide the design of high-performance NFAs.

Conflicts of interest

There are no conflicts to declare.

Acknowledgements

The authors acknowledge the financial support from Research Grant Council (RGC) of Hong Kong (General Research Fund No. 14303519) and NSFC/RGC Joint Research Scheme (Grant No.

N_CUHK418/17). X. Z. thanks NSFC (No. 51761165023). We gratefully thank Prof. Michael F. Toney with the open-source Matlab toolbox GIWAXS-SIIR kit for peak indexing of the GIWAXS pattern. We appreciate the fruitful discussions with Prof. Zengqi Xie and Dr Jiadong Zhou.

References

1 C. Q. Yan, S. Barlow, Z. H. Wang, H. Yan, A. K. Y. Jen, S. R. Marder and X. W. Zhan, *Nat. Rev. Mater.*, 2018, **3**, 18003.
2 J. Hou, O. Inganäs, R. H. Friend and F. Gao, *Nat. Mater.*, 2018, **17**, 119–128.
3 P. Cheng, G. Li, X. W. Zhan and Y. Yang, *Nat. Photonics*, 2018, **12**, 131–142.
4 L. X. Meng, Y. M. Zhang, X. J. Wan, C. X. Li, X. Zhang, Y. B. Wang, X. Ke, Z. Xiao, L. M. Ding, R. X. Xia, H. L. Yip, Y. Cao and Y. S. Chen, *Science*, 2018, **361**, 1094–1098.
5 D. Baran, T. Kirchartz, S. Wheeler, S. Dimitrov, M. Abdelsamie, J. Gorman, R. S. Ashraf, S. Holliday, A. Wadsworth, N. Gasparini, P. Kaienburg, H. Yan, A. Amassian, C. J. Brabec, J. R. Durrant and I. McCulloch, *Energy Environ. Sci.*, 2016, **9**, 3783–3793.
6 G. Li, R. Zhu and Y. Yang, *Nat. Photonics*, 2012, **6**, 153–161.
7 Y. H. Liu, J. B. Zhao, Z. K. Li, C. Mu, W. Ma, H. W. Hu, K. Jiang, H. R. Lin, H. Ade and H. Yan, *Nat. Commun.*, 2014, **5**, 1–8.
8 Y. Z. Lin, J. Y. Wang, Z. G. Zhang, H. T. Bai, Y. F. Li, D. B. Zhu and X. W. Zhan, *Adv. Mater.*, 2015, **27**, 1170–1174.
9 S. Q. Zhang, Y. P. Qin, J. Zhu and J. H. Hou, *Adv. Mater.*, 2018, **30**, 1800868.
10 H. Zhang, H. F. Yao, J. X. Hou, J. Zhu, J. Q. Zhang, W. N. Li, R. N. Yu, B. W. Gao, S. Q. Zhang and J. H. Hou, *Adv. Mater.*, 2018, **30**, 1800613.
11 D. He, F. W. Zhao, J. M. Xin, J. J. Rech, Z. X. Wei, W. Ma, W. You, B. Li, L. Jiang, Y. F. Li and C. R. Wang, *Adv. Energy Mater.*, 2018, **8**, 1802050.
12 T. Li, Y. Wu, J. Zhou, M. Li, J. Wu, Q. Hu, B. Jia, X. Pan, M. Zhang, Z. Tang, Z. Xie, T. P. Russell and X. Zhan, *J. Am. Chem. Soc.*, 2020, **142**, 20124–20133.
13 J. Yuan, Y. Q. Zhang, L. Y. Zhou, G. C. Zhang, H. L. Yip, T. K. Lau, X. H. Lu, C. Zhu, H. J. Peng, P. A. Johnson, M. Leclerc, Y. Cao, J. Ulanski, Y. F. Li and Y. P. Zou, *Joule*, 2019, **3**, 1140–1151.
14 R. Ma, T. Liu, Z. Luo, K. Gao, K. Chen, G. Zhang, W. Gao, Y. Xiao, T.-K. Lau and Q. Fan, *ACS Energy Lett.*, 2020, **5**, 2711–2720.
15 T. Liu, R. Ma, Z. Luo, Y. Guo, G. Zhang, Y. Xiao, T. Yang, Y. Chen, G. Li and Y. Yi, *Energy Environ. Sci.*, 2020, **13**, 2115–2123.
16 L. Zhan, S. Li, T.-K. Lau, Y. Cui, X. Lu, M. Shi, C.-Z. Li, H. Li, J. Hou and H. Chen, *Energy Environ. Sci.*, 2020, **13**, 635–645.
17 T. T. Yan, W. Song, J. M. Huang, R. X. Peng, L. K. Huang and Z. Y. Ge, *Adv. Mater.*, 2019, **31**, 1902210.
18 D. Q. Li, L. Zhu, X. J. Liu, W. Xiao, J. M. Yang, R. R. Ma, L. M. Ding, F. Liu, C. G. Duan, M. Fahlman and Q. Y. Bao, *Adv. Mater.*, 2020, **32**, 2002344.
19 S. Liu, J. Yuan, W. Deng, M. Luo, Y. Xie, Q. Liang, Y. Zou, Z. He, H. Wu and Y. Cao, *Nat. Photonics*, 2020, **14**, 300–305.
20 J. Yuan, C. J. Zhang, H. G. Chen, C. Zhu, S. H. Cheung, B. B. Qiu, F. F. Cai, Q. Y. Wei, W. Liu, H. Yin, R. Zhang, J. D. Zhang, Y. Liu, H. T. Zhang, W. F. Liu, H. J. Peng, J. L. Yang, L. Meng, F. Gao, S. K. So, Y. F. Li and Y. P. Zou, *Sci. China: Chem.*, 2020, **63**, 1159–1168.
21 Y. Cui, H. F. Yao, J. Q. Zhang, K. H. Xian, T. Zhang, L. Hong, Y. M. Wang, Y. Xu, K. Q. Ma, C. B. An, C. He, Z. X. Wei, F. Gao and J. H. Hou, *Adv. Mater.*, 2020, **32**, 1908205.
22 Y. Lin, Y. Firdaus, F. H. Isikgor, M. I. Nugraha, E. Yengel, G. T. Harrison, R. Hallani, A. El Labban, H. Faber and C. Ma, *ACS Energy Lett.*, 2020, **5**, 2935–2944.
23 Z. H. Luo, R. J. Ma, T. Liu, J. W. Yu, Y. Q. Xiao, R. Sun, G. S. Xie, J. Yuan, Y. Z. Chen, K. Chen, G. D. Chai, H. L. Sun, J. Min, J. Zhang, Y. P. Zou, C. L. Yang, X. H. Lu, F. Gao and H. Yan, *Joule*, 2020, **4**, 1236–1247.
24 B. B. Fan, D. F. Zhang, M. J. Li, W. K. Zhong, Z. M. Y. Zeng, L. Ying, F. Huang and Y. Cao, *Sci. China: Chem.*, 2019, **62**, 746–752.
25 Y. B. Lin, Y. Firdaus, F. H. Isikgor, M. I. Nugraha, E. Yengel, G. T. Harrison, R. Hallani, A. El-Labban, H. Faber, C. Ma, X. P. Zheng, A. Subbiah, C. T. Howells, O. M. Bakr, I. McCulloch, S. De Wolf, L. Tsetseris and T. D. Anthopoulos, *ACS Energy Lett.*, 2020, **5**, 2935–2944.
26 J. Q. Mai, Y. Q. Xiao, G. D. Zhou, J. Y. Wang, J. S. Zhu, N. Zhao, X. W. Zhan and X. H. Lu, *Adv. Mater.*, 2018, **30**, 1802888.
27 Y. Xiao, R. Ma, G. Zhou, J. Zhu, T.-K. Lau, S. Dai, J. J. Rech, N. Zhao, W. You, H. Yan, X. Zhan and X. Lu, *ACS Appl. Energy Mater.*, 2020, **3**, 10814–10822.
28 L. Zhu, M. Zhang, G. Q. Zhou, T. Y. Hao, J. Q. Xu, J. Wang, C. Q. Qiu, N. Prine, J. Ali, W. Feng, X. D. Gu, Z. F. Ma, Z. Tang, H. M. Zhu, L. Ying, Y. M. Zhang and F. Liu, *Adv. Energy Mater.*, 2020, **10**, 1904234.
29 G. Zhang, X. K. Chen, J. Xiao, P. C. Y. Chow, M. Ren, G. Kupgan, X. Jiao, C. C. S. Chan, X. Du, R. Xia, Z. Chen, J. Yuan, Y. Zhang, S. Zhang, Y. Liu, Y. Zou, H. Yan, K. S. Wong, V. Coropceanu, N. Li, C. J. Brabec, J. L. Bredas, H. L. Yip and Y. Cao, *Nat. Commun.*, 2020, **11**, 3943.
30 F. Lin, K. Jiang, W. Kaminsky, Z. Zhu and A. K. Y. Jen, *J. Am. Chem. Soc.*, 2020, **142**, 15246–15251.
31 X. H. Lu, H. Hlaing, D. S. Germack, J. Peet, W. H. Jo, D. Andrienko, K. Kremer and B. M. Ocko, *Nat. Commun.*, 2012, **3**, 1–7.
32 C. H. Su, U. Jeng, S. H. Chen, S. J. Lin, Y. T. Ou, W. T. Chuang and A. C. Su, *Macromolecules*, 2008, **41**, 7630–7636.
33 F. W. Zhao, C. R. Wang and X. W. Zhan, *Adv. Energy Mater.*, 2018, **8**, 1703147.
34 S. H. Chen, H. L. Chou, A. C. Su and S. A. Chen, *Macromolecules*, 2004, **37**, 6833–6838.
35 L. Ciammaruchi, O. Zapata-Arteaga, E. Gutiérrez-Fernández, J. Martin and M. Campoy-Quiles, *Mater. Adv.*, 2020, **1**, 2846–2861.
36 G. E. Wnek, *J. Chem. Educ.*, 2017, **94**, 1647–1654.

37 S. J. Wang, S. C. Yuan, K. Wang, W. Chen, K. Yamada, D. Barkley, T. Koga, Y. L. Hong and T. Miyoshi, *Macromolecules*, 2019, **52**, 4739–4748.
38 L. Y. Yu, D. P. Qian, S. Marina, F. A. A. Nugroho, A. Sharma, S. Hultmark, A. I. Hofmann, R. Kroon, J. Benduhn, D. M. Smilgies, K. Vandewal, M. R. Andersson, C. Langhammer, J. Martin, F. Gao and C. Muller, *ACS Appl. Mater. Interfaces*, 2019, **11**, 21766–21774.
39 Y. Z. Lin, Q. He, F. W. Zhao, L. J. Huo, J. Q. Mai, X. H. Lu, C. J. Su, T. F. Li, J. Y. Wang, J. S. Zhu, Y. M. Sun, C. R. Wang and X. W. Zhan, *J. Am. Chem. Soc.*, 2016, **138**, 2973–2976.
40 N. A. Ran, S. Roland, J. A. Love, V. Savikhin, C. J. Takacs, Y. T. Fu, H. Li, V. Coropceanu, X. F. Liu, J. L. Bredas, G. C. Bazan, M. F. Toney, D. Neher and T. Q. Nguyen, *Nat. Commun.*, 2017, **8**, 1–9.
41 W. Li, M. X. Chen, J. L. Cai, E. L. K. Spooner, H. J. Zhang, R. S. Gurney, D. Liu, Z. Xiao, D. G. Lidzey, L. M. Ding and T. Wang, *Joule*, 2019, **3**, 819–833.
42 J. Rivnay, S. C. B. Mannsfeld, C. E. Miller, A. Salleo and M. F. Toney, *Chem. Rev.*, 2012, **112**, 5488–5519.
43 V. Savikhin, H. G. Steinrück, R. Z. Liang, B. A. Collins, S. D. Oosterhout, P. M. Beaujuge and M. F. Toney, *J. Appl. Crystallogr.*, 2020, **53**, 1108–1129.
44 H. Sirringhaus, P. J. Brown, R. H. Friend, M. M. Nielsen, K. Bechgaard, B. M. W. Langeveld-Voss, A. J. H. Spiering, R. A. J. Janssen, E. W. Meijer, P. Herwig and D. M. de Leeuw, *Nature*, 1999, **401**, 685–688.
45 C. M. Proctor, J. A. Love and T. Q. Nguyen, *Adv. Mater.*, 2014, **26**, 5957–5961.
46 R. J. Ma, G. Li, D. D. Li, T. Liu, Z. H. Luo, G. Y. Zhang, M. Zhang, Z. Y. Wang, S. W. Luo, T. Yang, F. Liu, H. Yan and B. Tang, *Sol. RRL*, 2020, **4**, 2000250.
47 K. Li, Y. Wu, Y. Tang, M. A. Pan, W. Ma, H. Fu, C. Zhan and J. Yao, *Adv. Energy Mater.*, 2019, **9**, 1901728.
48 K. Li, Y. Wu, X. Li, H. Fu and C. Zhan, *Sci. China: Chem.*, 2020, 1–7.
49 J. M. Topple, S. M. McAfee, G. C. Welch and I. G. Hill, *Org. Electron.*, 2015, **27**, 197–201.
50 Y. Xiao and X. Lu, *Mater. Today Nano*, 2019, **5**, 100030.
51 X. Xu, Y. Li and Q. Peng, *Nano Select*, 2020, **1**, 30–58.
52 C. Yan, R. Ma, G. Cai, T. Liu, J. Zhu, J. Wang, Y. Li, J. Huang, Z. Luo and Y. Xiao, *EcoMat*, 2020, **2**, e12061.
53 C. Sun, F. Pan, H. Bin, J. Zhang, L. Xue, B. Qiu, Z. Wei, Z.-G. Zhang and Y. Li, *Nat. Commun.*, 2018, **9**, 1–10.

